JGR Oceans

RESEARCH ARTICLE
10.1029/2020JC016068

Labrador Sea Water Transport Across the Charlie-Gibbs Fracture Zone

Afonso Gonçalves Neto[1], Jaime B. Palter[1], Amy Bower[2], Heather Furey[2], and Xiaobiao Xu[3]

[1]Graduate School of Oceanography, University of Rhode Island, South Kingstown, RI, USA, [2]Woods Hole Oceanographic Institution, Falmouth, MA, USA, [3]Center for Ocean-Atmospheric Prediction Studies, Florida State University, Tallahassee, FL, USA

Key Points:
- LSW transport at CGFZ is estimated to be 5.3 ± 2.9 Sv and 8.2 ± 4.1 Sv from altimetry and a model hindcast, respectively
- LSW transport at CGFZ is modulated primarily by current velocities on seasonal to interannual time scales
- LSW thickness modulates transport on longer time scales and is sensitive to deep convection in the Labrador Sea

Correspondence to:
A. Gonçalves Neto,
afonso@uri.edu

Citation:
Gonçalves Neto, A., Palter, J. B., Bower, A., Furey, H., & Xu, X. (2020). Labrador Sea Water transport across the Charlie-Gibbs Fracture Zone. *Journal of Geophysical Research: Oceans*, *125*, e2020JC016068. https://doi.org/10.1029/2020JC016068

Received 9 JAN 2020
Accepted 29 JUN 2020
Accepted article online 3 JUL 2020

Abstract Labrador Sea Water (LSW) is a major component of the deep limb of the Atlantic Meridional Overturning Circulation, yet LSW transport pathways and their variability lack a complete description. A portion of the LSW exported from the subpolar gyre is advected eastward along the North Atlantic Current and must contend with the Mid-Atlantic Ridge before reaching the eastern basins of the North Atlantic. Here, we analyze observations from a mooring array and satellite altimetry, together with outputs from a hindcast ocean model simulation, to estimate the mean transport of LSW across the Charlie-Gibbs Fracture Zone (CGFZ), a primary gateway for the eastward transport of the water mass. The LSW transport estimated from the 25-year altimetry record is 5.3 ± 2.9 Sv, where the error represents the combination of observational variability and the uncertainty in the projection of the surface velocities to the LSW layer. Current velocities modulate the interannual to higher-frequency variability of the LSW transport at the CGFZ, while the LSW thickness becomes important on longer time scales. The modeled mean LSW transport for 1993–2012 is higher than the estimate from altimetry, at 8.2 ± 4.1 Sv. The modeled LSW thickness decreases substantially at the CGFZ between 1996 and 2009, consistent with an observed decline in LSW volume in the Labrador Sea after 1994. We suggest that satellite altimetry and continuous hydrographic measurements in the central Labrador Sea, supplemented by profiles from Argo floats, could be sufficient to quantify the LSW transport at the CGFZ.

Plain Language Summary Wintertime cooling of the Labrador Sea creates a pool of dense water and a fast track for anthropogenic CO_2 to enter the deep ocean. Stored for up to centuries before the Labrador Sea Water returns to the surface, the carbon captured within this layer does not contribute to the greenhouse effect. Despite playing this important role in the climate system, we still lack a complete understanding of the circulation pathways and spreading rates of the Labrador Sea Water. Here, we combine information from ocean- and satellite-based sensors with ocean model outputs to assess the flow rate of Labrador Sea Water through a fracture in the Mid-Atlantic Ridge, the main gateway between the eastern and western basins of the North Atlantic. We find that the fluctuating speed of the Labrador Sea Water transport across the Mid-Atlantic Ridge can be effectively inferred from satellite-observed surface currents. Additionally, changes in wintertime conditions in the Labrador Sea water can perturb the spreading rates onto the eastern Atlantic. By combining satellite-based estimates of surface speed and subsurface estimates of the water properties from floating sensors, we can monitor the transport of the carbon-rich water from the Labrador Sea in a changing ocean.

1. Introduction

Labrador Sea Water (LSW) is a major component of the deep limb of the Atlantic Meridional Overturning Circulation (AMOC). It forms in the central Labrador Sea and in the Irminger Sea through open-ocean deep convection and fills a large volume of the Atlantic Ocean (Gebbie & Huybers, 2011; Pickart et al., 2003). This water mass is also oxygen rich and a major sink for anthropogenic carbon (Khatiwala et al., 2009, 2013; Sabine et al., 2004). Thus, understanding the circulation and variability of LSW is important for a number of climate and biogeochemical questions. Although anomalies of the LSW water properties have been shown to be swiftly advected southward along the western boundary of the North Atlantic (Le Bras et al., 2017), the connection between variability in LSW formation and export rates to the subtropics was recently called into question (Zou & Lozier, 2016; Zou et al., 2018). Such a disconnect could arise if the fraction of the LSW mixed

and advected eastward were to vary, perhaps due to interactions with the North Atlantic Current (NAC). Ultimately, this eastward LSW transport must contend with the Mid-Atlantic Ridge (MAR), which acts as a barrier to zonal transport. Zonal currents tend to get funneled through deep fracture zones in the ridge, as schematized in Figure 1 (Bower et al., 2002).

LSW is known to follow several pathways as it leaves the Labrador Sea. Some LSW remains in the subpolar gyre in a weak anticyclonic recirculation that enters the Irminger Sea (Lavender et al., 2000). Evidence for this pathway has been obtained from hydrographic measurements and the averaging of float trajectories (Lavender et al., 2005; Palter et al., 2008, 2016). Conversely, much of the LSW is exported within the Labrador Current (Palter et al., 2008) and flows southeastward toward Flemish Cap and the Grand Banks of Newfoundland following the 2,000-m isobath in the continental slope. The fate of LSW downstream of Flemish Cap and the Tail of the Grand Banks depends upon its interactions with the northeastward flowing Gulf Stream: LSW may continue southward along the western boundary or be advected into the interior of the basin along with the NAC, as shown by Bower et al. (2011). The eastward transport of LSW carries climatic signals from the Labrador Sea to the deep ocean and contributes to the lower limb of the Meridional Overturning Circulation (Desbruyères et al., 2013).

The presence of LSW in the eastern North Atlantic basin has been reported since early studies of middepth circulation in the North Atlantic (Cunningham & Haine, 1995; McCartney, 1992; Pingree, 1973; Sy et al., 1997; Talley & McCartney, 1982). Moreover, LSW has long been thought to preferably cross the MAR via the two deep valleys of the Charlie-Gibbs Fracture Zone (CGFZ), the largest geological fault in the North Atlantic portion of the MAR (Paillet et al., 1998; Wright & Worthington, 1970). The CGFZ is, indeed, a major water mass crossroads, as it funnels both the eastward flowing LSW and other water masses carried by the NAC at surface and intermediate depths, and the westward flowing Iceland Scotland Overflow Water (ISOW) in the deepest layers of the water column (Bower & Furey, 2017; Saunders, 1994). In addition, the LSW contributes to the dilution of the ISOW in this region (Racapé et al., 2019). Early efforts to quantify the LSW geostrophic transport through the MAR used hydrographic data and provided estimates that range from 4 to 13 Sv (Paillet et al., 1998; Schmitz & McCartney, 1993; Worthington, 1976). Though these studies have revealed much about the mean LSW transport into the eastern North Atlantic basin, its temporal variability is yet to be explored.

Continuous observational efforts to understand the rates and variability of LSW formation and transport have been made in regions such as the central Labrador Sea (e.g., Yashayaev & Loder, 2016) and along the perimeter of the North American continent: the western Labrador Sea at 53°N (e.g., Fischer et al., 2010; Zantopp et al., 2017), the Tail of the Grand Banks (e.g., Schott et al., 2006), and south of New England (e.g., Toole et al., 2017). However, we lack continuous measurements of the eastward transport of LSW across the MAR. We aim to fill this gap with a combination of 22 months of direct measurements made by moorings in the CGFZ, inferences from altimetry, and a regional ocean circulation model that has been widely validated for its faithful representation of circulation in this region (Xu et al., 2013). Characterizing the variability of the LSW transport through the CGFZ will contribute to the understanding of the water mass propagation downstream from the formation region.

In the following section, we describe the mooring array (section 2.1), the altimetry data along with other observational data (section 2.2), and the ocean circulation model used in this study (section 2.3). The measurements recorded by the moored instruments are used to quantify the transport of LSW across the mooring array and characterize its variability over 22 months of direct observations (section 3.1). Next, the satellite-derived surface geostrophic velocities (section 3.2) and the model simulations (section 3.3) reveal the variability of the LSW transport at the CGFZ over the past three decades. Finally, we summarize and conclude our work with an outlook for the future (section 4).

2. Data and Methods

2.1. Moorings in the Western CGFZ

A mooring array was deployed in the CGFZ between 52°N and 53°N along a nominal longitude of 35.33°W to quantify the transport of ISOW (Bower & Furey, 2017). The array, deployed for 677 days between August 2010 and June 2012, consisted of eight moorings spanning from south of the fault ridge to the southern flank

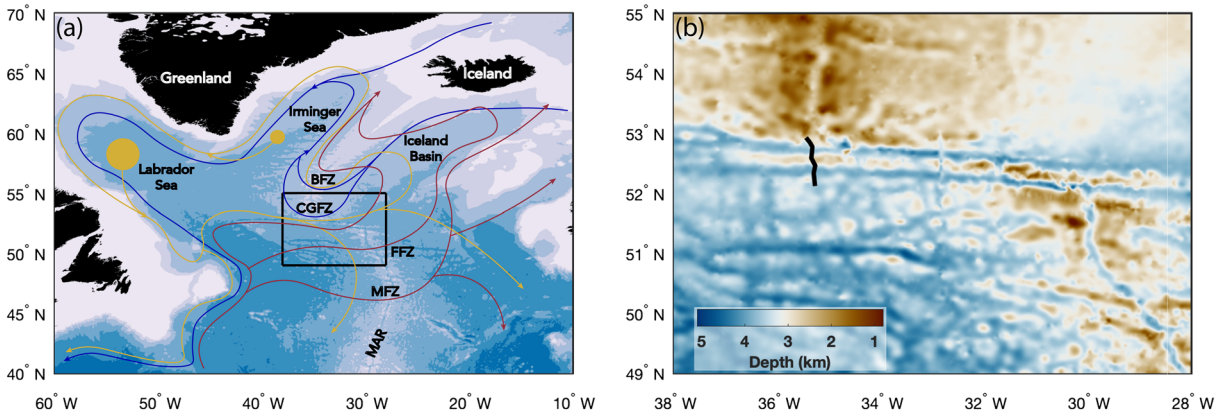

Figure 1. Circulation and bathymetry of the subpolar North Atlantic. (a) Schematic circulation diagram showing primary shallow (red) and deep (yellow and blue) currents in the subpolar North Atlantic. The LSW formation regions are shown as yellow circles, and its main pathways are indicated as yellow arrows. Abbreviations include Bight Fracture Zone (BFZ), Charlie-Gibbs Fracture Zone (CGFZ), Faraday Fracture Zone (FFZ), and Maxwell Fracture Zone (MFZ). (b) Detailed bathymetry at the Mid-Atlantic Ridge for the region that includes the Charlie-Gibbs Fracture Zone. The mooring array is indicated in black on the west side of the CGFZ.

of the Reykjanes Ridge. The four tall (seafloor to 500 m) and four short (seafloor to 1,500 m) moorings were deployed as shown on the meridional section in Figure 2, with letters A–H denoting the eight moorings at the top of panel (a). Temperature, conductivity, and pressure were recorded from 36 SBE-37 MicroCATs, while direct measurements of the velocity components were made with 28 current meters (18 Aanderaa RCM-11 and 10 Nortek AquaDopp 6000 DW). The mooring configuration and further details of the deployments can be found in Furey et al. (2014).

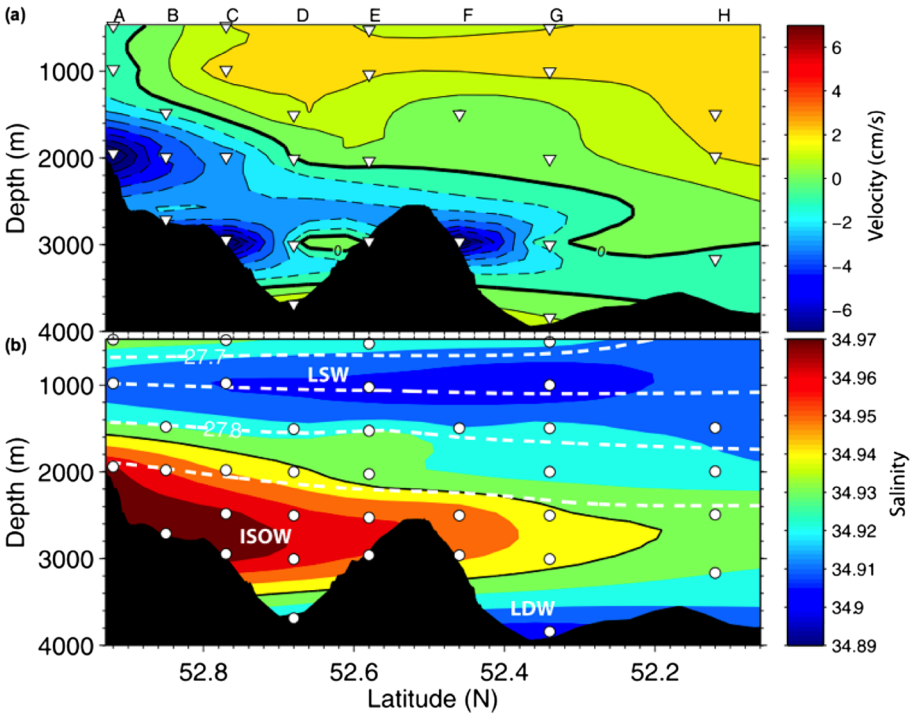

Figure 2. Zonal velocity and salinity at the CGFZ mooring array. (a) Cross section of time mean velocity from moored current meters. White triangles indicate the location of the current meters. Thick black line is the 0-cm s^{-1} isotach. Mooring labels are indicated on the top of the figure. (b) Similar to panel (a) but for salinity. White circles indicate the location of the MicroCats. Thick black line is the 34.94 isohaline. Dashed white lines are isopycnals. Mean locations of LSW, ISOW, and Lower Deep Water (LDW) are indicated. Figure from Bower and Furey (2017).

The methodology implemented to estimate the LSW transport across the mooring array follows the one described by Bower and Furey (2017), who used the same data set to quantify the volume transport in the ISOW layer. In their work, ISOW was defined as the waters with salinity greater than 34.94 g kg^{-1}. Here, we define LSW as the waters whose salinity is lower than 34.94 g kg^{-1} (Worthington, 1976) and σ_θ is between 27.68 and 27.80 kg m^{-3} (Schott et al., 2004; Stramma et al., 2004). As in Bower and Furey (2017), we filtered all data with a low-pass third-order Butterworth filter with a 40-hr cutoff period, run forward and backward in order to eliminate phase shifts.

Temperature and salinity were averaged daily and linearly interpolated vertically onto 1-m bins between the top and bottom MicroCATs for each mooring before potential density was calculated. When the 27.68-kg m^{-3} isopycnal was shallower than the shallowest instruments in the tall moorings, the top interface of the LSW was assumed to be 500 m. This occurred in 53% of the measurements at the tall moorings, and, as such, the LSW thickness may be slightly underestimated. Hydrographic sections and salinity observed at the mooring array suggest that the halocline consistently extends below 500 m, indicating that the 34.94 g kg^{-1} threshold is likely not far above the top instrument depth on the tall moorings (see Bower & Furey, 2017, Figures 3 and 5). Because the 27.68-kg m^{-3} isopycnal is always shallower than 1,500 m, the top interface of the LSW in the short moorings was calculated as the average depth of the 27.68-kg m^{-3} isopycnal in the two neighboring moorings. For Mooring H, the southernmost short mooring with only one neighbor to the north, the top interface was determined by mirroring Mooring G.

Similarly to temperature and salinity, the velocity components were averaged to daily values and linearly interpolated vertically onto 1-m bins between the top and bottom current meters in each mooring. As the moorings were deployed nearly along a line of constant longitude (35.33°W), the zonal component of the velocity field is approximately normal to the mooring array, and only this component is used further in the analysis. The daily LSW velocity across each mooring was calculated as the average of the zonal velocity between the top and bottom interfaces of the water mass. To deduce velocities at depths above the short moorings, we rely on the deduction from an empirical orthogonal function (EOF) analysis that most of the zonal velocity variability at the mooring array is explained by a vertical mode with very little shear (Bower & Furey, 2017). For this reason, the zonal velocity above 1,500 m was constructed by adding the time mean values of neighboring moorings and the fluctuations of the 1,500-m current meter at Moorings B, D, and F. At Mooring H, the top 1,000-m zonal velocity was calculated as the fluctuations of the 1,500-m current meter plus the time mean zonal velocity of Mooring G above 1,500 m.

The daily time series of LSW transport per unit width ($m^2\ s^{-1}$) across each mooring was then calculated by multiplying the mean zonal velocity between the top and bottom interfaces of the LSW layer by the LSW thickness (i.e., the distance between the two interfaces). Finally, this transport was multiplied by the distance separating the midpoints between adjacent moorings to arrive at a volume transport in sverdrups. For Moorings A and H, this value was calculated as the distance between the moorings and their closest neighbor. Because the LSW always resided above the shallowest bathymetry of the CGFZ, no transport needed to be estimated between an instrument and adjacent bathymetry. The time series of LSW properties are filtered with a low-pass third-order Butterworth filter with a 30-day cutoff to remove the signals from high-frequency (weekly or shorter) variability.

It is important to note that the original purpose of the mooring array was to quantify ISOW transport across the CGFZ. Because the CGFZ is a transform fault, the position of the ridge crest is shifted on either side of the fracture zone: North of the CGFZ, the ridge crest aligns with 35°W, and south of the ridge crest it lies nearly along 30°W (Figure 4). As the moorings were deployed at 35°W, they are only situated in a true ridge gap in the north valley, where they are bounded by the Reykjanes Ridge to the north and the transform ridge to the south. In contrast, the moorings south of the transform ridge are about 3° to the west of the MAR and have no bounding bathymetric feature directly to the south. This placement of the mooring array was designed to investigate the westward transport of ISOW into the western basin (Bower & Furey, 2017). Unfortunately, the placement is less ideal for quantifying the eastward flow of LSW across the CGFZ, given that the eastward currents can meander south of the mooring array and still cross the MAR through the CGFZ. Because of this limitation, and to consider variability in CGFZ transport at time scales longer than 2 years, we turn to satellite altimetry and an ocean model in sections 3.2 and 3.3, respectively.

2.2. Satellite Altimetry and Other Observational Data

The Global Ocean Gridded L4 Sea Surface Height product was obtained from the Copernicus Marine Environment Monitoring Service (CMEMS). The 0.25° × 0.25° daily gridded data set is a multimission altimeter product that combines data from multiple satellites, including Topex/Poseidon, Jason-1, and Jason-2. Data released include the daily surface geostrophic currents with the same 0.25° × 0.25° resolution, derived from the lateral gradient of the absolute dynamic topography. The gridded absolute dynamic topography and the surface geostrophic velocities from January 1993 to December 2017 were used to determine the mean position of the northern branch of the NAC in the region between 50°N and 55°N, 29°W and 38°W, which shed light on the importance of calculating the LSW transport farther east from the mooring array, at 32°W.

The zonal geostrophic velocity was interpolated onto two sections: the first at the mooring array (35.33°W) and the second along 32°W. Bower and Furey (2017) showed that the leading vertical mode of the zonal velocity was equivalent-barotropic, explaining 68–74% of the variance. The next leading mode, explaining 21–27% of the remaining variance, was the first baroclinic mode, which changed sign beneath the base of the LSW layer. Therefore, the mooring observations suggest that the LSW velocity should covary with the surface velocity, and we confirm this relationship by calculating a linear regression between the surface and the LSW velocities at the moorings. Our goal was to build a proxy for LSW transport based on altimetry, thus allowing for the investigation of LSW velocity variability over the 25-year altimetry era at the center of the fault ridge, 3° to the east of the mooring array.

We calculated the ratio of LSW layer velocity to the surface geostrophic velocity using two observational products in addition to that calculated from the 22-month LSW velocity from the mooring array compared against the colocated surface geostrophic velocities. In the first estimate, the vertical zonal velocity shear between surface and LSW layer depth (nominally 1,000 m) was calculated by applying the thermal wind equation to a climatological density field. We used the Australia's Commonwealth Scientific and Industrial Research Organisation (CSIRO) Atlas of Regional Seas (CARS2009), a product with a 0.5° horizontal resolution and 79 vertical levels spanning from surface to 5,500 m (Dunn & Ridgway, 2002). The CARS2009 data product was created with a modified Loess filter to interpolate the irregularly spaced observations into a regular grid. This scheme uses a bathymetry-influenced weighting, which more accurately preserves gradients in areas with steep topography such as the MAR; as such, we believe it to be an appropriate climatology for our purposes.

In the second estimate, the 1,000-dbar time mean velocity field was calculated based on float displacements for the Argo era. The Argo data set is freely available by the International Argo Program (http://www.argo.ucsd.edu). The 1,000-dbar float displacements were then compared to surface pseudodisplacements calculated from altimetric geostrophic velocities interpolated to the starting position of each float displacement with the method described by Willis and Fu (2008).

2.3. Numerical Simulation

A (1/12)° eddying simulation based on the HYbrid Coordinate Ocean Model (HYCOM) was used to explore LSW transport variability in 1978–2012 and the role of variable LSW thickness and velocity in the transport variability. The model configuration has been described in Xu et al. (2013), who also provided several detailed model-data comparisons in the subpolar North Atlantic. The model results are shown to realistically simulate the observed time mean structure of the western boundary current transport off the Labrador Coast, as well as the warming and sea surface height change in the central Labrador Sea since the early 1990s. Additionally, the model exhibits almost no salinity drift, with a slow increase rate of only 0.02 per century. More recently, Xu et al. (2018) examined the westward ISOW transport through the CGFZ and showed that the simulation reproduced most of the intraseasonal to interannual variability observed in the moored current meter arrays during 1988–1989 (Saunders, 1994) and 2010–2012 (Bower & Furey, 2017).

The model outputs include potential temperature, salinity, and the zonal and meridional velocities. LSW thickness was determined as the layer whose σ_θ is between 27.68 and 27.80 kg m^{-3}. A third-order Butterworth low-pass filter with a 30-day cutoff, run forward and backward in order to eliminate phase shifts, was applied to emphasize variability at time scales longer than one month.

3. Key Results

3.1. LSW Transport at the CGFZ Mooring Array

Temperature and salinity observations reveal the key water masses situated along the mooring array (Figure 2). The LSW lies on top of the ISOW in the north valley and on the southern flank of the zonally oriented transform ridge. Further south, the lower layer is filled with cold, fresh Lower Deep Water (LDW), a water mass that is thought to be a mixture of Antarctic Bottom Water and North Atlantic Deep Waters (McCartney, 1992; Saunders, 1994). The surface layer is dominated by warmer waters that are generally advected and mixed to the east by the NAC and its eddies (Bower & Furey, 2017).

The mean zonal LSW transport measured across the mooring array was 1.9 ± 2.3 Sv, where the reported uncertainty is 1 standard deviation. Transport measured at Moorings F–H, located south of the transform ridge, contributed the majority of the transport 1.3 ± 2.6 Sv. In the north valley, Moorings C–E also recorded eastward mean transport in the LSW layer and contributed 0.7 ± 1.6 Sv. The mean eastward LSW transport is not ubiquitous throughout the array, as transport at the northernmost Moorings A and B, located on the southern flank of the Reykjanes Ridge, averages -0.1 ± 0.6 Sv. In addition to this spatial variability, the LSW thickness and velocity also have strong temporal variability at the mooring array.

During the mooring deployment, several periods of elevated eastward flow were observed, the strongest of which reached 7 Sv between the autumn of 2011 and the winter of 2012 (Figure 3e). The three periods of strong eastward transport, all surpassing 4 Sv, were associated with two distinct spatial distributions of the thickness and velocity anomaly fields across the mooring array, respectively, shown in Figures 3a and 3c. During the winters of 2010/2011 and 2011/2012, positive thickness and eastward velocity anomalies are measured at all moorings, with peak velocities in the north valley. In contrast, in the summer of 2011, strong positive thickness and eastward velocity anomalies are measured in the south valley, while negative thickness and westward velocity anomalies are observed in the north valley.

In contrast, the transport time series reveals that there were also periods of weak westward LSW transport averaged over the whole array during four events, collectively lasting about one fifth of the deployment period. These events were each driven by slightly different spatial configurations of the velocity field. In November–December 2010, the longest westward event, strong westward velocity anomalies are measured by the southern moorings, while eastward anomalies are observed in the north valley. In April 2011, February–March 2012, and May 2012, westward velocity anomalies are measured across most of the array. The anomalous westward velocities are associated with negative thickness anomalies during all of these events (Figures 3a and 3c).

The transport variability over the 22-month deployment period is almost entirely controlled by the zonal velocity in the LSW layer, which explains 98% of its variability. The 30-day low-passed LSW thickness and zonal velocity averaged over the mooring array are shown in blue and green, respectively, in Figure 3e. The mean thickness is $1{,}069 \pm 73$ m, and single daily mean values range from 900 to 1,230 m. On average, there is a meridional thickness gradient along the array, with thicker LSW at Mooring H (1,202 m), thinning northward to Mooring A (867 m, Figure 3b). The zonal velocity during the 22 months averages 1.4 ± 1.8 cm s^{-1}, ranging from -3.0 cm s^{-1} (westward) to 6.7 cm s^{-1} (eastward).

As noted in section 2.1 above, the mooring array does not capture the maximum eastward velocities that cross the MAR at the CGFZ. A map of the mean surface circulation from satellite altimetry (Figure 4) shows that the average position of the maximum surface eastward velocity is south of the mooring array. Therefore, the red line positioned further east in Figure 4, at 32°W, represents a more ideal location for the quantification of the eastward transport across the CGFZ. We next attempt to quantify the LSW transport variability across the CGFZ at this line, as described in the following sections.

3.2. Circulation Variability at the CGFZ From Altimetry

Sea surface geostrophic velocities calculated from satellite altimetry are significantly correlated with LSW velocities at the mooring array. The ratio between surface and LSW velocities at the mooring array is 0.27 and the correlation coefficient between the two is 0.51. In the north valley, the satellite-observed surface velocities and the LSW velocities are more strongly connected, with correlation coefficient rising to 0.81, averaged over Moorings A through E only. The north valley is bounded by steep topography to both the

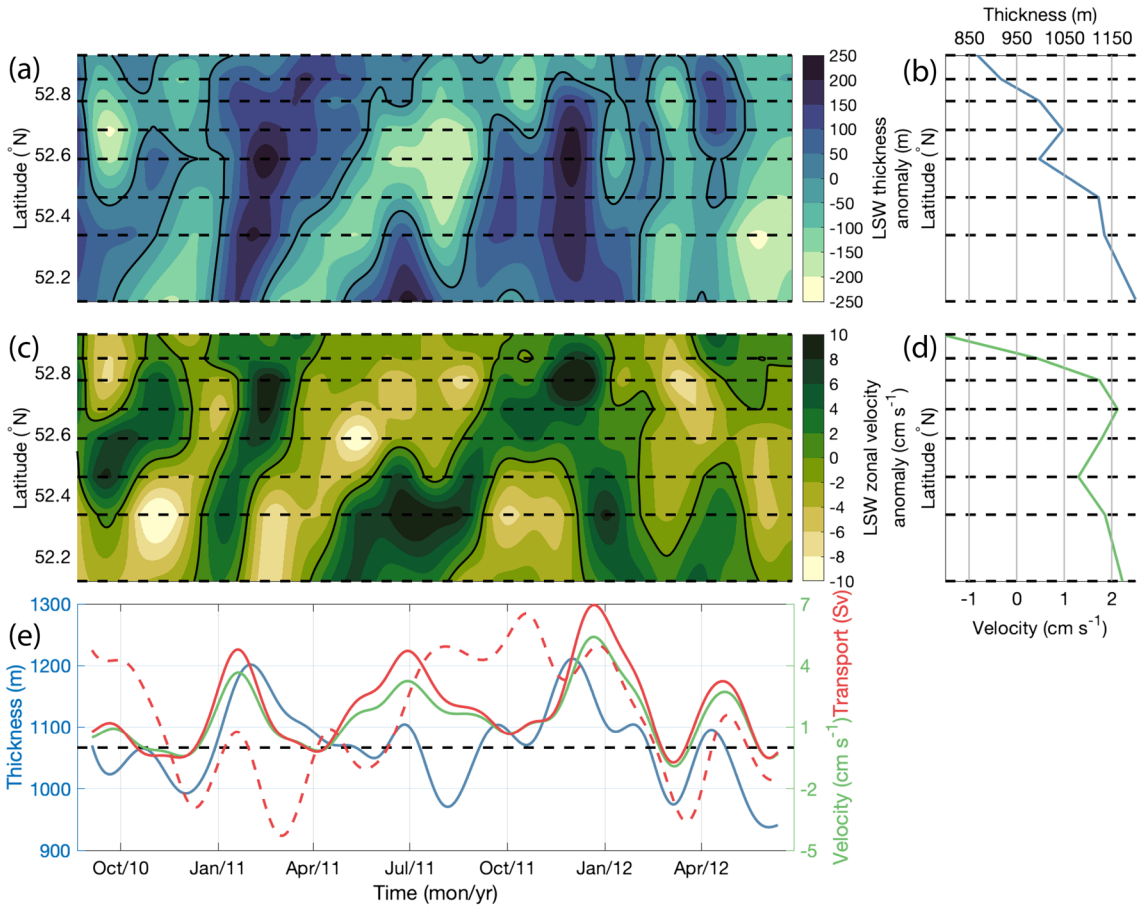

Figure 3. LSW properties and transport at the mooring array. (a) The 22-month Hovmöller diagram of the 30-day low-passed LSW thickness anomaly at the mooring array. The latitude of each mooring (A is the northernmost) is shown as dashed lines. Thick black line is the 0-m thickness anomaly contour. (b) The 22-month mean LSW thickness across the mooring array. Dashed lines indicate the latitude of each mooring. (c) LSW zonal velocity anomaly through the mooring array, with same plotting conventions as in panel (a). Thick black line is the 0-cm s^{-1} zonal velocity anomaly contour. (d) The 22-month mean LSW zonal velocity. (e) The 22-month time series of the 30-day low-passed LSW thickness (blue), zonal velocity (green), and zonal transport (red) averaged across the eight moorings. The red lines, whose correlation coefficient R is equal to 0.33, are the transport as calculated from the moored instruments (solid) and the model output interpolated to the mooring positions (dashed). The dashed black line denotes LSW zonal velocity and transport equal to 0.

north and south and thus has similar bathymetric constraints on the NAC as those the current experiences where it crosses the CGFZ at 32°W. A visual comparison between observed surface and LSW velocities shows that strong events of eastward LSW transport are associated with the swift eastward surface velocities (Figures 3c and 5). Likewise, the westward LSW transport anomalies correspond with westward anomalies in surface velocities. The strong relationship between the altimetric surface velocities and LSW layer velocities, particularly in the bathymetrically constrained north valley, suggests that the altimeter record can provide an indicator of temporal variability in the LSW layer velocity as it crosses the CGFZ.

Figure 6 shows the mean total (light lines) and cumulative (dark lines) LSW transport in 0.5° bins between 53°N and 40°N. In red, we show this transport at 35°W, and in black interpolated to the center of the MAR rift valley. This figure is made from observational data: LSW thickness estimated from the CARS climatology and the LSW layer velocity from the objectively mapped ARGO displacements at 1,000 dbar. The LSW transport is clearly much higher at the CGFZ than elsewhere along the MAR, peaking at 3.2 Sv at 52°N. The latitudinal band of the CGFZ, between 51.5°N and 53°N, accounts for 66% of the total eastward transport of LSW over the MAR (7.8 Sv across the CGFZ vs. 11.8 Sv total). If we include the Faraday Fracture Zone (extending the southern limit to 50°N), this value goes to 85%. We chose to estimate the LSW transport at the latitude band of 51.7°N to 53°N because we were limited by the location of the mooring array and the spatial extent of the region where the estimated vertical shear is relatively constant. Finally, it is

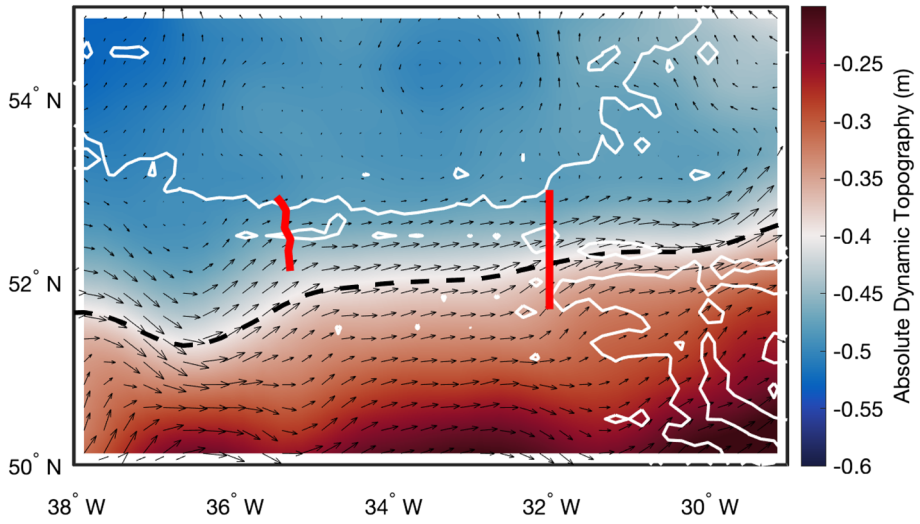

Figure 4. Mean surface geostrophic velocity (arrows) overlaying the mean dynamic topography (colors) in the CGFZ region. The red line to the left indicates the locations of the eight moorings. The black dashed line is the mean position of the 39.5-cm ADT isoline, which coincides with the maximum surface velocities associated with the northern branch of the NAC. A more ideal position for the quantification of LSW transport across the CGFZ is also shown in red, shifted 3° to the east of the moorings. This line is located at the mean position of the ridge crest at the latitude band of the CGFZ, as calculated from ETOPO1 (Amante & Eakins, 2009). It is bounded by the 3,000-m isobath to both the north and south and extends from 51.7°N to 53°N. The 3,000-m isobath is shown as a white contour.

important to note that over 40% of the eastward LSW transport that crosses 35°W is recirculated southward along the western flank of the MAR and does not cross into the eastern basin, as shown by comparing red and black lines in Figure 6.

To understand whether the surface geostrophic velocity may serve as a proxy for the LSW layer velocity at 32°W, where the swiftest eastward velocity crosses the MAR (see Figure 4), we must first assess whether the vertical shear between the surface and LSW layer is similar to that observed at the mooring array at 35°W. To do so, we compare the vertical shear calculated at the moorings to the shear at 32°W using two different, independent, observation-based techniques and checking the relationship in a model simulation.

First, we compared the subsurface displacements of Argo floats drifting at 1,000 dbar, the approximate center of the LSW layer at the CGFZ, to surface pseudotrajectories constructed by interpolating the altimetric geostrophic velocities to the time and location of the floats, as was done in Willis and Fu (2008) and Palter et al. (2016). All subsurface float trajectories were gathered in 1° bins and regressed against the surface

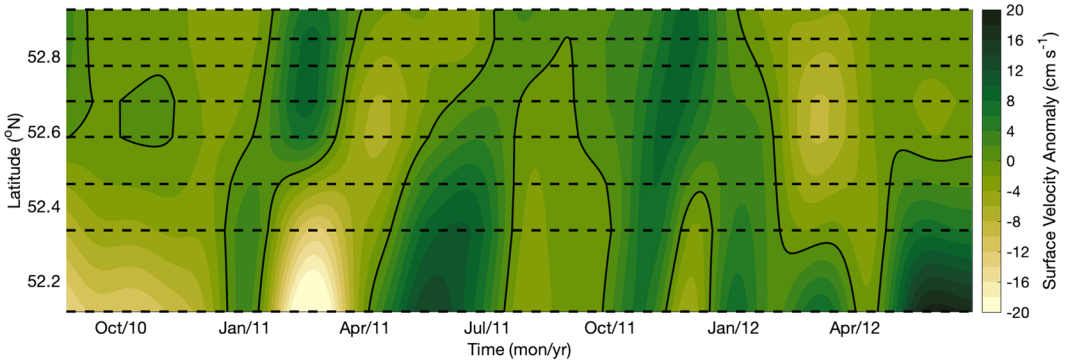

Figure 5. Twenty-two month Hovmöller diagram of the 30-day low-passed zonal surface geostrophic velocity anomaly at the location of the mooring array. The solid black contour is the 0-cm s^{-1} velocity anomaly. Dashed lines indicate the latitude of each mooring.

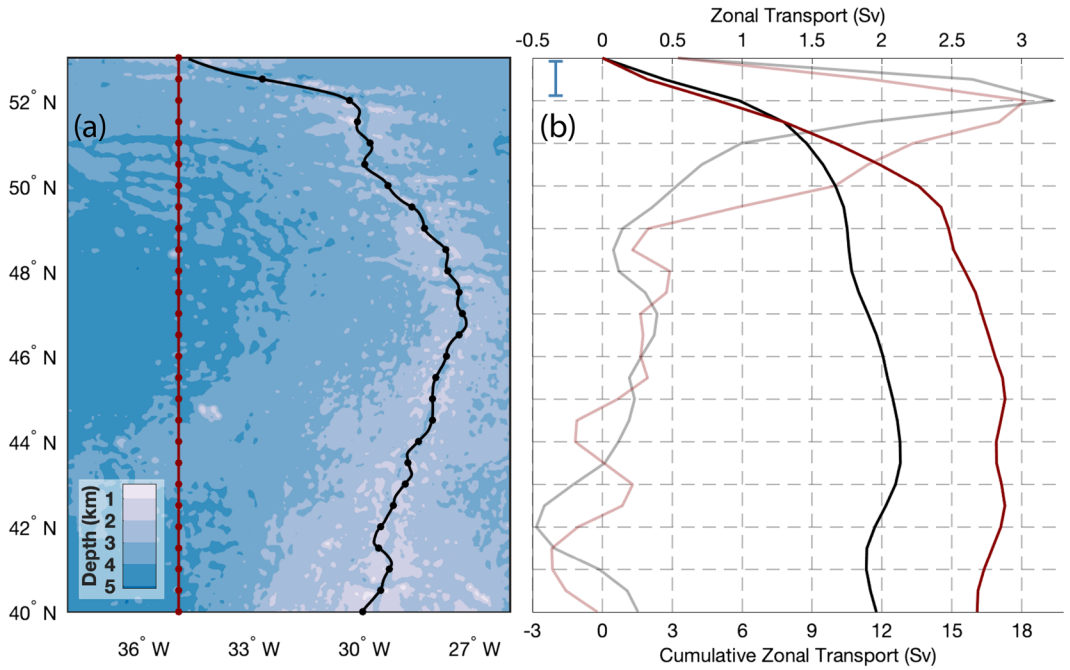

Figure 6. Eastward transport of LSW through the Mid-Atlantic Ridge. (a) Bathymetry map of the Mid-Atlantic Ridge between 40°N and 53°N, showing the 35°W line (red) and the center of the Mid-Atlantic Ridge rift valley (black). Dots represent the grid points at which the lines in panel b were calculated, with a 0.5° latitudinal resolution. (b) Total (light lines) and cumulative (dark lines) zonal transport of LSW at 35°W (red) and the Mid-Atlantic Ridge rift valley (black), as estimated from the CARS climatology (LSW thickness) and Argo/PALACE floats displacements (1,000-dbar velocity). The latitude band of the mooring array is indicated in blue.

pseudotrajectories, yielding a regression coefficient that represents the ratio of the 1,000-dbar velocity to the surface velocity. Between the bin encompassing the mooring location (centered at 35°W, 52°N) and the bin encompassing the location of maximum cross-MAR surface velocities (32°W, 52°N), this ratio varies between 0.22 and 0.31. The number of trajectories in each bin used to calculate this regression ranges between 65 and 82.

Second, the geostrophic (i.e., thermal wind) shear from the climatological density field was used to calculate the velocity difference between the surface and 1,000 m. We found that the thermal wind shear is relatively constant over a zonally elongated band at the CGFZ, with the ratio of the 1,000-m velocities to surface velocities ranging from 0.53 at 35°W to 0.57 at 32°W.

Finally, we also compare the surface velocity to the LSW layer velocity in the model, as discussed in more detail in the next section. In brief, the model relationship is consistent with the Argo- and mooring-based estimates of the shear, with the ratio between LSW and surface zonal velocities of 0.19. It is notable that the geostrophic shear inferred from the climatological meridional density gradient is at least 2 times weaker than the float-, mooring-, and model-based shear estimates. We therefore suspect that the smoothed climatological product underestimates the meridional density gradients over the scale of interest. Yet we incorporate the full range of observation-based estimates of the ratio between surface and LSW layer velocities (0.22–0.57) into a conservative metric of the uncertainty of the calculated LSW velocity. In practice, the total uncertainty of the LSW velocity at 32°W is calculated as $\sigma_{U_{lsw}} = \sqrt{\sigma^2_{shear} + \sigma^2_{U_{geo}}}$, where σ_{shear} and $\sigma_{U_{geo}}$ are, respectively, the uncertainty of the vertical velocity shear, described here, and the standard deviation of the surface geostrophic velocities.

The mean surface zonal velocity at 32°W, shown in Figure 7, is about twice as fast as at the location of the mooring array ($7.9 \pm 4.7\,\mathrm{cm\,s^{-1}}$ vs. $3.9 \pm 2.7\,\mathrm{cm\,s^{-1}}$), averaged over the approximately 25-year altimetric record. Surface currents across the CGFZ show intense variability at time scales ranging from intraseasonal to decadal, as seen from the monthly (thin line) and 1-year (thick line) low-passed time series. The maximum

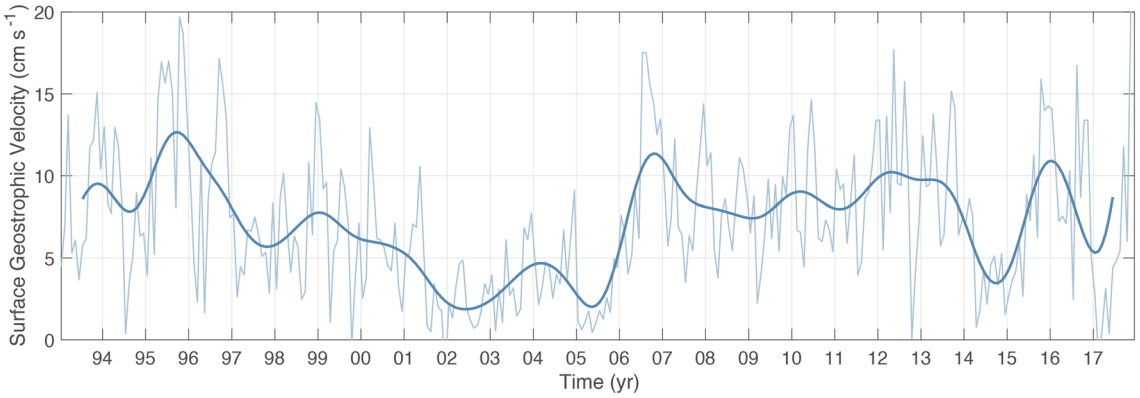

Figure 7. Time series of monthly (thin line) and 1-year low-passed zonal surface geostrophic velocity at the CGFZ (32°W).

cross-CGFZ annual mean velocity exceeds 13 cm s^{-1} in 1995, after which there is a slow decline to a 5-year period of annual mean velocity of less than 5 cm s^{-1} between 2001 and 2005, with a record minimum of 3 cm s^{-1} in 2002. By 2006, annual mean velocities recovered to about 10 cm s^{-1}, and averaged 9 cm s^{-1} until the end of the delayed-time available at the time of writing.

Given that the moorings show that LSW velocity is correlated with the surface geostrophic velocity, as was also implied by the strongly barotropic nature of the flow (Bower & Furey, 2017), and having assessed the uncertainty on the vertical velocity shear between 32°W and 35°W, we can infer the variability of the LSW velocity through the CGFZ. Strong eastward LSW velocity events likely occurred in the early 1990s and after 2006, while weak eastward velocity and possibly westward reversals were likely between 2001 and 2006. Using the shear calculated from the comparison of the surface geostrophic velocity and LSW layer velocity at the mooring array, as well as the two other observational shear assessments, we estimate that the mean LSW velocity for the altimetric era is 3.4 ± 1.8 cm s^{-1}. Assuming a constant LSW thickness of 1,069 m, which is the time-averaged LSW thickness calculated from the mooring measurements, we estimate that the LSW volume transport at the CGFZ averages 5.3 ± 2.9 Sv.

Having observed that thickness variability contributes little to the LSW transport variability over the 22-month mooring array, it is tempting to assume that the surface geostrophic velocities can accurately represent the LSW volume transport and that the time series in Figure 7 is a good multidecadal record of LSW transport variability. However, we next show in section 3.3 that this assumption may not hold on longer time scales.

3.3. Model-Based LSW Transport Across the CGFZ

The modeled time mean LSW transport at the location of the mooring array between August 2010 and June 2012 is 1.4 ± 3.4 Sv, compared to 1.9 ± 2.3 Sv estimated from the observations. The lower transport in the model is due to the fact the model maximum eastward flow is located slightly to the south of that observed. The variability of the modeled and observed LSW transport through the CGFZ is displayed in Figure 3e. There is some similarity between the model and observations but the agreement is not as good as in the ISOW as shown in Xu et al. (2018). This may not be surprising, since the mooring array captured only the northern edge of the eastward flow of LSW but the entire westward flow of ISOW.

Figure 8 compares the mean LSW thickness derived from CARS (Ridgway et al., 2002) and the 1,000-dbar velocity derived from Argo displacements (Palter et al., 2016) and the modeled LSW thickness and velocity. The LSW is overall thicker in the model than in observations. However, there is similarity in the spatial pattern between model results and observations: the LSW is thick in the Irminger Sea and very thin above the Reykjanes Ridge. South of the Reykjanes Ridge, in the western basin, the LSW flows eastward toward the MAR providing the thick layer that is observed at the CGFZ. Likewise, in both observations and the model, the LSW zonal velocity is notably higher at the latitude of the CGFZ than elsewhere along the MAR, with a maximum that resembles the mean meridional position of the northern branch of the NAC shown in Figure 4.

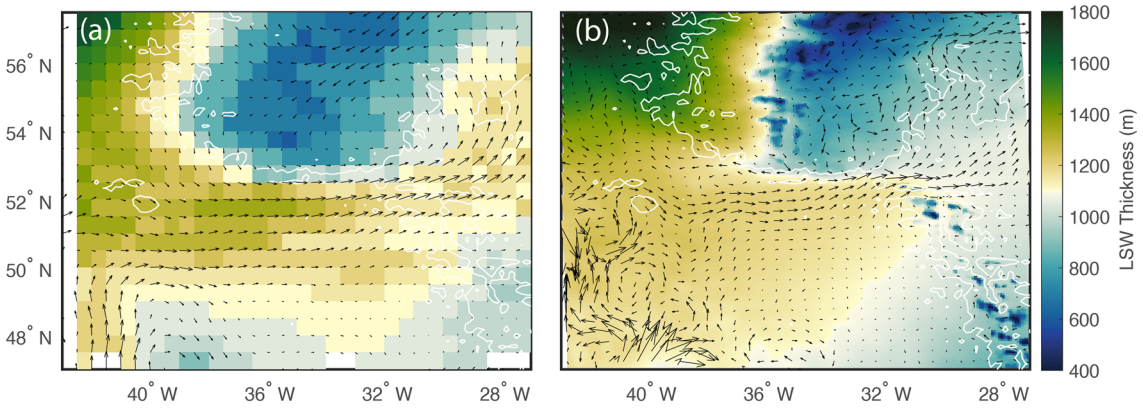

Figure 8. Maps of mean LSW thickness and velocity. (a) Observed climatological mean LSW thickness calculated from CARS2009 gridded temperature and salinity, and velocities derived from the Eulerian averaging of Argo and PALACE 1000 dbar float displacements. (b) Mean LSW thickness and velocities for 2010–2012 from the model output.

The modeled LSW transport at 32°W between 1978 and 2012 was 9.0 ± 4.4 Sv, about 70% larger than the 5.3 Sv estimated in observations for 1993–2017. This is due to both a thicker LSW layer and higher velocity in model results. However, comparing only the time period in which observations and the model overlap, the LSW transport is reduced to 8.2 ± 4.1 Sv, as the LSW thickness and velocity in the model are closer to those in the observed estimates. The model LSW thickness averages (±1 standard deviation) 1,246 ± 32 m over 2010–2012 (compared to the mooring-based thickness of 1,069 ± 73 m), and the simulated velocity is 4.0 ± 2.1 cm s^{-1} after 1993 (compared to 3.4 ± 1.8 cm s^{-1} inferred from the altimetry-based surface velocity and the three observational estimates of vertical shear). The differences between the modeled and observed LSW thickness and velocity are greater when comparing the entire time period in the simulation, as the observational period saw a thinner LSW layer and slower velocity than earlier in the simulation.

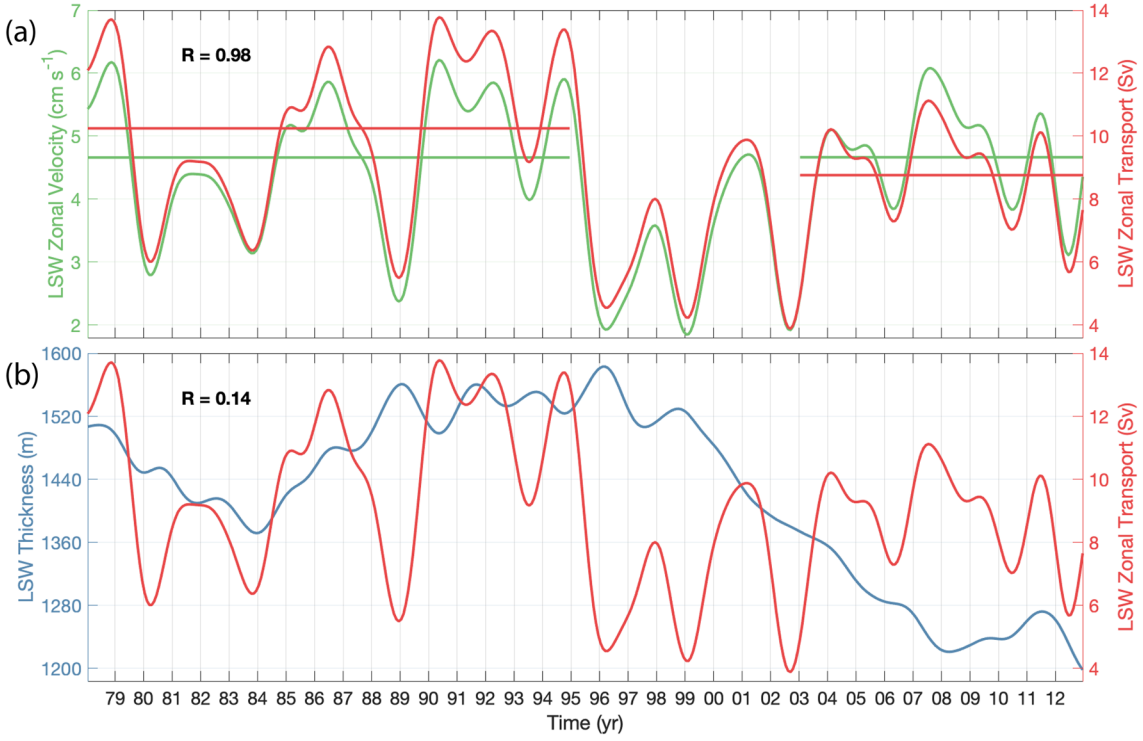

Figure 9. Model time series of LSW at CGFZ. (a) Zonal LSW velocity (green) and zonal LSW transport (red) at the CGFZ (32°W) in the model simulation from 1978 to 2012. The mean LSW velocity and transport for 1978–1994 (4.7 cm s^{-1}, 10.2 Sv) and 2003–2012 (4.6 cm s^{-1}, 8.7 Sv) are shown as straight lines. (b) Similar to a) except that the blue line is the LSW thickness.

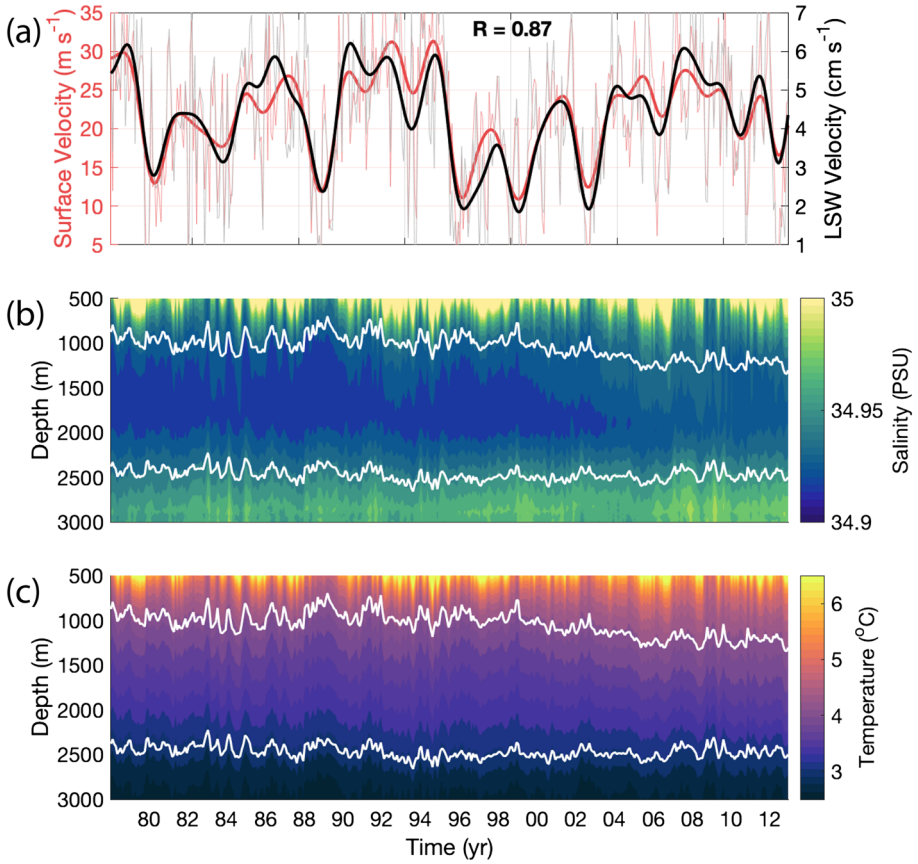

Figure 10. Modeled velocity, salinity, and temperature at CGFZ from 1978 to 2012. (a) Time series of surface (red) and LSW (black) velocities. Thin lines are the monthly time series and thick lines are the low-passed time series with one year cutoff. The correlation coefficient between the two time series is given in the panel. (b) Hovmöller diagram of salinity. White lines indicate the upper and lower limits of the LSW layer. (c) Same as middle panel, except for temperature.

As in the mooring observations, the LSW transport variability is mostly explained by changes in LSW velocity (96%) with a minor contribution from LSW thickness. Figure 9 shows the time series of LSW transport through the CGFZ as compared with the LSW velocity (top panel) and the LSW thickness (bottom panel). The monthly mean LSW velocity and thickness vary considerably during the entire period. Velocity fluctuations drive the monthly to interannual LSW transport variability. In the mid-1990s, both velocity and transport declined by nearly two thirds over the course of 2 years, during an anomalous period of reduced LSW transport through the CGFZ.

The results from the model output indicate that LSW thickness can be important on longer time scales. Prior to 1995, LSW transport across the CGFZ averaged 10.2 Sv. An abrupt decrease in LSW velocity in 1995 decreased the transport to 6.9 Sv between 1996 and 2003. After 2003, the velocity increased again to reach rates equal to the ones observed before 1995, but the transport did not recover to its pre-1995 average. The mean velocity during the last available decade (2003–2012) is 4.6 cm s^{-1}, statistically equal to the 4.7 cm s^{-1} simulated before 1995 (T test, 95% significance level). The transport, however, averaged 8.7 Sv after 2003, which is statistically lower than the mean 10.2 Sv before 1995, (T test, 95% significance level). This is explained by a continuous decrease in the LSW thickness between the mid-1990s and the mid-2000s that greatly impacts its total transport. The LSW was consistently thicker before 1999, with annual averages above 1,500 m between 1991 and 1999 and dropped to less than 1,300 m by 2005. Therefore, shifts in LSW thickness have to be taken into consideration when inferring the cross-CGFZ LSW transport variability on decadal and longer time scales. Although the short-term variability in the LSW transport across the

CGFZ is modulated very little by the thickness, a long-term thinning of the water mass reduces the volume of LSW crossing the CGFZ from 2003 to 2012.

The LSW velocity and thickness at the CGFZ vary on different time scales. Figure 10a reveals that the LSW velocity is highly correlated with the surface velocity (R=0.87), similar to the relationship inferred from the mooring array and satellite altimetry. The LSW thickness is, by definition, controlled by the temperature and salinity stratification. These characteristics changed within the LSW layer after the mid-1990s. The fresh core of the LSW has become saltier, as the 34.92 isohaline vanished in 2007 after continuously thinning since 1999 (Figure 10b). The isotherms deepened and resulted in a warmer LSW, particularly after 2006 (Figure 10c).

4. Discussion and Conclusions

This study quantified the LSW transport across the CGFZ and explored its substantial temporal variability. Data from a mooring array at the western edge of the CGFZ were used to investigate the transport of LSW and its relationship with surface geostrophic currents in the region. However, the mean position of the northern branch of the NAC, the main driver of the LSW transport across the CGFZ, is located to the south of the mooring array. The NAC turns slightly northward east of the mooring array before crossing the MAR to the eastern basin. The mean surface velocity at the mooring array location is about half as strong as that at the center of the NAC. Therefore, we use altimetry to estimate the LSW transport where the swiftest cross-MAR eastward velocities are found. This approach depends on the assumption that the velocities in the LSW layer are strongly correlated to the surface layer and that the vertical shear between the surface and LSW velocities can be deduced from existing data. The mooring array and numerical model simulation suggests that altimetric surface geostrophic velocities are well correlated with velocities on the LSW layer. Moreover, there is strong agreement in the vertical shear estimated from the mooring data and from the regression with hundreds of Argo float displacement velocities at 1,000 m compared to the altimetric geostrophic surface velocities. The shear simulated in the model is also in close agreement with these two estimates. We therefore argue that surface geostrophic velocities can be used to create a proxy for LSW velocity.

The swift surface geostrophic velocities at the CGFZ at 32°W coincides with a thick layer of LSW (Figures 4 and 8), suggesting that this is the location of maximum eastward LSW transport across the MAR. At this ridge gap, the surface geostrophic velocity for the altimetric era varies strongly on intraseasonal to decadal time scales. The meridional excursion of the NAC at the MAR sets the boundary between the North Atlantic subpolar and subtropical gyres and has been extensively investigated in a number of observational (Bower & von Appen, 2008; Rhein et al., 2011; Roessler et al., 2015) and modeling (Breckenfelder et al., 2017) analyses. The LSW transport at CGFZ is locally controlled by changes in the NAC velocities on intraseasonal to interannual time scales. The meridional excursion of the NAC—and therefore its position relative to the CGFZ—is in turn associated with fluctuations in the zonal wind stress in the western European Basin east of the CGFZ (Bower & Furey, 2017; Xu et al., 2018). Assuming constant LSW thickness and using the calculated vertical shear of the zonal velocity, we estimated the altimetry-derived LSW transport through the CGFZ to be 5.3 $\pm$ 2.9 Sv.

Although fluctuations in the velocity field explain much of the LSW transport variability through the CGFZ on interannual and shorter time scales, the spatial and temporal variability of the LSW thickness must be accounted for when addressing the total LSW transport across the MAR. The model simulation indicates that the LSW thickness may play an important role in modulating LSW transport on decadal time scales. The simulation shows continuous thinning of the LSW layer between 1996 and 2009 at the CGFZ, during a time when velocities were recovering following a sharp slowdown in 1995. Thus, the LSW transport does not increase over the 13-year period as the velocity alone would imply (Figure 9).

LSW thickness at the CGFZ appears to be controlled by remote variations in LSW formation. Direct observations along the AR7 W hydrographic section across the central Labrador Sea have shown that deep convection reached a depth of 2,400 m between 1987 and 1994, forming a thick layer of dense LSW (Curry et al., 1998; Yashayaev et al., 2007). Following this maximum, the formation of denser LSW was suppressed for over a decade (Azetsu-Scott et al., 2003; Yashayaev et al., 2007). In the Labrador Sea, the shallower convection after 1994 was responsible for at least 1,000 m of thinning of the newly formed LSW after 1994 (Kieke &

Yashayaev, 2015; Rhein et al., 2011, 2017). Subsequent thinning of the LSW was observed in mooring arrays and hydrographic sections downstream of the Labrador Sea along the Deep Western Boundary Current between 56°N and 39°N (Le Bras et al., 2017; Stramma et al., 2004). At CGFZ, our model accurately simulates the trend on the LSW layer thickness observed upstream (Figure 9b).

The model used here also faithfully simulates the observed warming of the LSW layer along the AR7 W section associated with the reduction in deep convection that started in 1994 (see Figure 4 in Xu et al., 2013). The transit time from the Labrador Sea to the CGFZ has been evaluated by tracing newly formed LSW with temperature, salinity, and chlorofluorocarbon (CFC) concentration anomalies (Sy et al., 1997). They found that newly formed LSW reaches the Iceland Basin within 2 to 3.5 years. Consistent with that approximate timing, the simulated LSW thickness at the CGFZ peaks in 1996 (Figure 9), 2 years after its peak thickness in the Labrador Sea (Xu et al., 2013; Yashayaev & Loder, 2016). Reduced convection and associated warming in the Labrador Sea is followed by a deepening of the isotherms and salinification of the LSW core at the CGFZ beginning in the mid-1990s (Figure 10).

The suite of observed and modeled evidence presented here suggests that the LSW transport at CGFZ varies in response to both fluctuations of the NAC velocity, which modulates the interannual to higher-frequency variability and remote changes in LSW formation in the central Labrador Sea, which can give rise to decadal variability of the transport. Exposing the substantial variability in the eastward transport of LSW across the MAR also points toward additional open questions about both the causes and consequences of such variability. For instance, it is interesting to consider whether large-scale wind patterns and convection in the LSW formation region covary, potentially causing changes in the volume and properties of exported LSW as well as its export pathways. Moreover, it remains unknown how variability in the LSW transport across the CGFZ may influence heat transport and stratification in the eastern basin, where ocean to atmosphere heat fluxes strongly influence regional climate. This work suggests that future efforts to quantify the eastward LSW transport across the CGFZ can take advantage of the relationship between surface and LSW layer velocities, as long as a temporally evolving estimate of LSW thickness can be resolved from hydrographic and Argo data.

Data Availability Statement

The mooring data presented in this paper are available from NCEI (http://accession.nodc.noaa.gov/0164585). The model outputs are stored in the U.S. Navy DSRC archive server, and the model results presented in this study are available in HYCOM server (ftp://ftp.hycom.org/pub/xbxu/ATLg0.08/CGFZ). The AVISO altimeter data were downloaded from the Copernicus Marine Environment Monitoring Service website (http://marine.copernicus.eu/services-portfolio/access-to-products/). The CARS2009 data were downloaded from the Commonwealth Scientific and Industrial Research Organisation (http://www.marine.csiro.au/~dunn/cars2009/). The Argo profile data were downloaded from the Argo website (http://www.argo.ucsd.edu/).

Acknowledgments
The authors thank Dr. Virginie Thierry and one anonymous reviewer for the insightful comments and suggestions. A. G. N. appreciates conversations with Kathy Donohue, Tom Rossby and Lisa Beal, which helped to interpret the results. J. B. P. acknowledges support from NSF through Grant OCE-1947829. The authors thank all colleagues and ship crew involved in the R/V Meteor cruise M-82/2 and Maria S. Merian cruise MSM-21/2. The mooring data presented in this paper were funded by NSF through Grant OCE-0926656.

References

Amante, C., & Eakins, B. W. (2009). ETOPO1 1 arc-minute global relief model: Procedures, data sources and analysis. NOAA Technical Memorandum NESDIS NGDC-24, National Geophysical Data Center, NOAA.

Azetsu-Scott, K., Jones, E. P., & Yashayaev, I. (2003). Time series study of CFC concentrations in the Labrador Sea during deep and shallow convection regimes (1991–2000). *Journal of Geophysical Research*, *108*(C11), 1–8. https://doi.org/10.1029/2002JC001317

Bower, A., & Furey, H. (2017). Iceland-Scotland Overflow Water transport variability through the Charlie-Gibbs Fracture Zone and the impact of the North Atlantic Current. *Journal of Geophysical Research: Oceans*, *122*, 6989–7012. https://doi.org/10.1002/2017JC012698

Bower, A., Le Cann, B., Rossby, T., Zenk, W., Gould, J., Speer, K., et al. (2002). Directly measured mid-depth circulation in the northeastern North Atlantic Ocean. *Nature*, *419*, 603–607. https://doi.org/10.1038/nature01078

Bower, A., Lozier, S., & Gary, S. (2011). Export of Labrador Sea Water from the subpolar North Atlantic: A Lagrangian perspective. *Deep-Sea Research Part II: Topical Studies in Oceanography*, *58*(17-18), 1798–1818. https://doi.org/10.1016/j.dsr2.2010.10.060

Bower, A., & von Appen, W.-J. (2008). Interannual variability in the pathways of the North Atlantic Current over the Mid-Atlantic Ridge and the impact of topography. *Journal of Physical Oceanography*, *38*, 104–120. https://doi.org/10.1175/2007JPO3686.1

Breckenfelder, T., Rhein, M., Roessler, A., Böning, C. W., Biastoch, A., Behrens, E., & Mertens, C. (2017). Flow paths and variability of the North Atlantic Current: A comparison of observations and a high-resolution model. *Journal of Geophysical Research: Oceans*, *122*, 2686–2708. https://doi.org/10.1002/2016JC012444

Cunningham, S. A., & Haine, T. W. N. (1995). Labrador Sea Water in the eastern North Atlantic. Part I: A synoptic circulation inferred from a minimum in potential vorticity. *Journal of Physical Oceanography*, *25*, 649–665. https://doi.org/10.1175/1520-0485(1995)025<0649:LSWITE>2.0.CO;2

Curry, R. G., McCartney, M. S., & Joyce, T. M. (1998). Oceanic transport of subpolar climate signals to mid-depth subtropical waters. *Nature*, *391*(6667), 575–577. https://doi.org/10.1029/2012JC008342

Desbruyères, D., Thierry, V., & Mercier, H. (2013). Simulated decadal variability of the meridional overturning circulation across the A25-Ovide section. *Journal of Geophysical Research: Oceans*, *118*, 462–475. https://doi.org/10.1029/2012JC008342

Dunn, J. R., & Ridgway, K. R. (2002). Mapping ocean properties in regions of complex topography. *Deep-Sea Research Part I*, *49*, 591–604. https://doi.org/10.1016/S0967-0637(01)00069-3

Fischer, J., Visbeck, M., Zantopp, R., & Nunes, N. (2010). Interannual to decadal variability of outflow from the Labrador Sea. *Geophysical Research Letters*, *37*, 1–5. https://doi.org/10.1029/2010GL045321

Furey, H. H., Trafford, L., & Bower, A. S. (2014). A crossroads of the Atlantic Meridional Overturning Circulation: The Charlie-Gibbs Fracture Zone data report August 2010–June 2012. Woods Hole, Massachussets: Woods Hole Oceanographic Institution.

Gebbie, G., & Huybers, P. (2011). How is the ocean filled? *Geophysical Research Letters*, *38*, L06604. https://doi.org/10.1029/2011GL046769

Khatiwala, S., Primeau, F., & Hall, T. (2009). Reconstruction of the history of anthropogenic CO_2 concentrations in the ocean. *Nature*, *462*(7271), 346–349. https://doi.org/10.1038/nature08526

Khatiwala, S., Tanhua, T., Mikaloff Fletcher, S., Gerber, M., Doney, S. C., Graven, H. D., et al. (2013). Global ocean storage of anthropogenic carbon. *Biogeosciences*, *10*(4), 2169–2191. https://doi.org/10.5194/bg-10-2169-2013

Kieke, D., & Yashayaev, I. (2015). Studies of Labrador Sea Water formation and variability in the subpolar North Atlantic in the light of international partnership and collaboration. *Progress in Oceanography*, *132*, 220–232. https://doi.org/10.1016/j.pocean.2014.12.010

Lavender, K., Davis, R., & Owens, W. (2000). Mid-depth recirculation observed in the interior Labrador and Irminger seas by direct velocity measurements. *Nature*, *407*(6800), 66–69. https://doi.org/10.1038/35024048

Lavender, K., Owens, W. B., & Davis, R. E. (2005). The mid-depth circulation of the subpolar North Atlantic Ocean as measured by sub-surface floats. *Deep-Sea Research Part I*, *52*, 767–785. https://doi.org/10.1016/j.dsr.2004.12.007

Le Bras, I. A., Yashayaev, I., & Toole, J. M. (2017). Tracking Labrador Sea Water property signals along the Deep Western Boundary Current. *Journal of Geophysical Research: Oceans*, *122*, 5348–5366. https://doi.org/10.1002/2017JC012921

McCartney, M. S. (1992). Recirculating components to the deep boundary current of the northern North Atlantic. *Progress in Oceanography*, *29*, 283–383. https://doi.org/10.1016/0079-6611(92)90006-L

Paillet, J., Arhan, M., & McCartney, M. S. (1998). Spreading of Labrador Sea Water in the eastern North Atlantic. *Journal of Geophysical Research*, *103*(98), 10223. https://doi.org/10.1029/98JC00262

Palter, J. B., Caron, C.-A., Law, K. L., Willis, J. K., Trossman, D. S., Yashayaev, I. M., & Gilbert, D. (2016). Variability of the directly observed, middepth subpolar North Atlantic circulation. *Geophysical Research Letters*, *43*, 2700–2708. https://doi.org/10.1002/2015GL067235

Palter, J. B., Lozier, M. S., & Lavender, K. L. (2008). How does Labrador Sea Water enter the deep western boundary current? *Journal of Physical Oceanography*, *38*(5), 968–983. https://doi.org/10.1175/2007JPO3807.1

Pickart, R. S., Straneo, F., & Moore, G. W. K. (2003). Is Labrador Sea Water formed in the Irminger basin? *Deep-Sea Research Part I: Oceanographic Research Papers*, *50*(1), 23–52. https://doi.org/10.1016/S0967-0637(02)00134-6

Pingree, R. D. (1973). A component of Labrador Sea Water in the Bay of Biscay. *Limnology and Oceanography*, *18*(5), 711–718. https://doi.org/10.4319/lo.1973.18.5.0711

Racapé, V., Thierry, V., Mercier, H., & Cabanes, C. (2019). ISOW spreading and mixing as revealed by Deep-Argo floats launched in the Charlie Gibbs Fracture Zone. *Journal of Geophysical Research: Oceans*, *124*, 6787–6808. https://doi.org/10.1029/2019JC015040

Rhein, M., Kieke, D., Sabine, H., Roessler, A., Mertens, C., Yashayaev, I., et al. (2011). Deep water formation, the subpolar gyre, and the meridional overturning circulation in the subpolar North Atlantic. *Deep-Sea Research Part II*, *58*, 1819–1832. https://doi.org/10.1016/j.dsr2.2010.10.061

Rhein, M., Steinfeldt, R., Kieke, D., Stendardo, I., & Yashayaev, I. (2017). Ventilation variability of Labrador Sea Water and its impact on oxygen and anthropogenic carbon: A review. *Phylosophycal Transactions A*, *375*, 1–17. https://doi.org/10.1098/rsta.2016.0321

Ridgway, K. R., Dunn, J. R., & Wilkin, J. L. (2002). Ocean interpolation by four-dimensional weighted least squares application to the waters around Australasia. *Journal of Atmospheric and Oceanic Technology*, *19*, 1357–1375. https://doi.org/10.1175/1520-0426(2002)019<1357:OIBFDW>2.0.CO;2

Roessler, A., Rhein, M., Kieke, D., & Mertens, C. (2015). Long-term observations of North Atlantic Current transport at the gateway between western and eastern Atlantic. *Journal of Geophysical Research: Oceans*, *120*, 4003–4027. https://doi.org/10.1002/2014JC010662

Sabine, C. L., Feely, R. A., Gruber, N., Key, R. M., Lee, K., Bullister, J. L., et al. (2004). The oceanic sink for anthropogenic CO_2. *Science*, *305*(5682), 367–371. https://doi.org/10.1126/science.1097403

Saunders, P. M. (1994). The flux of overflow water through the Charlie-Gibbs Fracture Zone. *Journal of Geophysical Research*, *99*(C6), 12,343–12,355. https://doi.org/10.1029/94jc00527

Schmitz, W. J., & McCartney, M. S. (1993). On the North Atlantic Circulation. *Reviews of Geophysics*, *31*(1), 29–49. https://doi.org/10.1029/92RG02583

Schott, F. A., Fischer, J., Dengler, M., & Zantopp, R. (2006). Variability of the deep western boundary current east of the grand banks. *Geophysical Research Letters*, *33*, L21S07. https://doi.org/10.1029/2006GL026563

Schott, F. A., Zantopp, R., Stramma, L., Dengler, M., Fischer, J., & Wibaux, M. (2004). Circulation and deep-water export at the western exit of the subpolar North Atlantic. *Journal of Physical Oceanography*, *34*(2004), 817–843. https://doi.org/10.1175/1520-0485(2004)034<0817:CADEAT>2.0.CO;2

Stramma, L., Kieke, D., Rhein, M., Schott, F., Yashayaev, I., & Koltermann, K. P. (2004). Deep water changes at the western boundary of the subpolar North Atlantic during 1996 to 2001. *Deep-Sea Research Part I: Oceanographic Research Papers*, *51*(8), 1033–1056. https://doi.org/10.1016/j.dsr.2004.04.001

Sy, A., Rhein, M., Lazier, J. R. N., Koltermann, K. P., Meincke, J., Putzka, A., & Bersch, M. (1997). Surprisingly rapid spreading of newly formed intermediate waters across the North Atlantic Ocean. *Nature*, *386*(6626), 675–679. https://doi.org/10.1038/386675a0

Talley, L. D., & McCartney, M. S. (1982). Distribution and circulation of Labrador Sea Water. *Journal of Physical Oceanography*, *12*(11), 1189–1205. https://doi.org/10.1175/1520-0485(1982)012<1189:DACOLS>2.0.CO;2

Toole, J. M., Andres, M., Le Bras, I. A., Joyce, T. M., & McCartney, M. S. (2017). Moored observations of the deep western boundary current in the NW Atlantic: 2004–2014. *Journal of Geophysical Research: Oceans*, *122*, 7488–7505. https://doi.org/10.1002/2017JC012984

Willis, J. K., & Fu, L. L. (2008). Combining altimeter and subsurface float data to estimate the time-averaged circulation in the upper ocean. *Journal of Geophysical Research*, *113*, C12017. https://doi.org/10.1029/2007JC004690

Worthington, L. V. (1976). On the North Atlantic circulation. *The Johns Hopkins Oceanographic Studies*, *6*, 110.

Wright, W. R., & Worthington, L. V. (1970). North Atlantic Ocean atlas of potential temperature and salinity in the deep water. *Woods Hole Oceanographic Institution Atlas Series 2*, *2*, 24.

Xu, X., Bower, A., Furey, H., & Chassignet, E. (2018). Variability of the Iceland-Scotland overflow water transport through the Charlie-Gibbs Fracture Zone: Results from an eddying simulation and observations. *Journal of Geophysical Research: Oceans*, *123*, 5808–5823. https://doi.org/10.1029/2018JC013895

Xu, X., Hurlburt, H. E., Schmitz, W. J., Zantopp, R., Fischer, J., & Hogan, P. J. (2013). On the currents and transports connected with the atlantic meridional overturning circulation in the subpolar North Atlantic. *Journal of Geophysical Research: Oceans*, *118*, 502–516. https://doi.org/10.1002/jgrc.20065

Yashayaev, I., Bersch, M., & van Aken, H. M. (2007). Spreading of the Labrador Sea Water to the Irminger and Iceland basins. *Geophysical Research Letters*, *34*, L10602. https://doi.org/10.1029/2006GL028999

Yashayaev, I., & Loder, J. W. (2016). Recurrent replenishment of Labrador Sea Water and associated decadal-scale variability. *Journal of Geophysical Research: Oceans*, *121*, 8095–8114. https://doi.org/10.1002/2016JC012046

Zantopp, R., Fischer, J., Visbeck, M., & Karstensen, J. (2017). From interannual to decadal: 17 years of boundary current transports at the exit of the Labrador Sea. *Journal of Geophysical Research: Oceans*, *122*, 1724–1748. https://doi.org/10.1002/2016JC012271

Zou, S., & Lozier, M. S. (2016). Breaking the linkage between Labrador Sea Water production and its advective export to the subtropical gyre. *Journal of Physical Oceanography*, *46*, 2169–2182. https://doi.org/10.1175/JPO-D-15-0210.1

Zou, S., Lozier, M. S., & Buckley, M. W. (2018). How is meridional coherence maintained in the lower limb of the Atlantic Meridional Overturning Circulation? *Geophysical Research Letters*, *45*, 244–252. https://doi.org/10.1029/2018GL080958